

Response of Local Evanescent Array-Coupled Biosensors to Organic Nanofilms

Rongjin Yan, *Student Member, IEEE*, Santano P. Mestas, *Student Member, IEEE*, Guangwei Yuan, Rashid Safaisini, *Student Member, IEEE*, and Kevin L. Lear, *Member, IEEE*

Abstract—A label-free planar optical waveguide immunosensor that operates on the novel principle of local evanescent field shift is demonstrated in this paper. Increased local refractive index at the waveguide's upper surface due to the formation of an organic adlayer shifts the evanescent field distribution up, and hence, changes the light intensity both above and below the waveguide structure. Beam propagation simulations show increased modulation ratio sensitivity to adlayer thickness with increasing detection distance below the waveguide. The local nature of detection allows sensors to be implemented in array formats on a single waveguide for multiple-analyte sensing. Both near-field scanning optical microscopy and integrated buried detector arrays are employed to study the response to patterned organic nanofilms including immunocomplexes, photoresist, and adsorbed bovine serum albumin (BSA) layers. Buried polysilicon detector arrays integrated with silicon nitride waveguides in a commercial CMOS process exhibit a 15% photocurrent modulation ratio response to an approximately 1-nm-thick adsorbed film of BSA. CMOS compatibility enables a low-cost sensor system on a chip. Temperature dependence measurements show that sensor has a 0.3%/°C change in modulation ratio, which is thousands of times less than traditional resonant biosensors.

Index Terms—CMOS optoelectronics, immunosensor, integrated optical waveguide biosensor, near-field scanning optical microscopy (NSOM).

I. INTRODUCTION

A VARIETY of label-free photonic biosensors have been widely studied in recent years, because they provide a relatively easy and inexpensive way to detect molecular interactions and quantify their kinetics [1]–[4]. Among different detection mechanisms, one of the most popular methods is measuring a guided optical mode's modulation induced by the refractive index change associated with specific binding of molecules in the mode's evanescent field with no need for fluorescent labeling. Many biosensors based on binding in evanescent fields provide very high sensitivities, including surface plasmon resonance (SPR) biosensors [5]–[7] and microring resonator biosensors proposed by Boyd and Heebner [8] and devel-

Manuscript received January 6, 2009; revised February 13, 2009. First published June 16, 2009; current version published October 7, 2009. This work was supported in part by National Institutes of Health under Grant EB00726 and by the National Science Foundation (NSF) under Grant ESC0323493. S. P. Mestas was supported by the NSF Bridge to Doctorate Fellowship.

R. Yan, G. Yuan, and R. Safaisini are with the Department of Electrical and Computer Engineering, Colorado State University, Fort Collins, CO 80523 USA (e-mail: yanrj@engr.colostate.edu).

S. P. Mestas and K. L. Lear are with the Department of Electrical and Computer Engineering and the School of Biomedical Engineering, Colorado State University, Fort Collins, CO 80523 USA (e-mail: kevin.lear@colostate.edu).

Color versions of one or more of the figures in this paper are available online at <http://ieeexplore.ieee.org>.

Digital Object Identifier 10.1109/JSTQE.2009.2017207

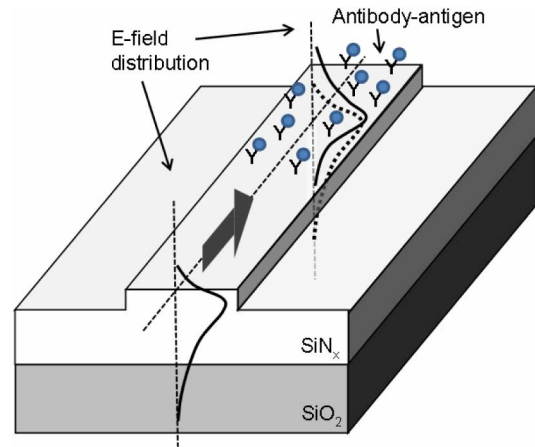


Fig. 1. LEAC sensor concept: the E -field shifts up when light propagates into a waveguide region covered by an adlayer. Immobilization of molecular probes such as antibodies on the waveguide surface allows sensitive detection of target molecules such as antigens via specific binding.

oped by various groups [9]–[11]. However, in most of these sensors, the modification of the transmitted optical mode's phase or amplitude is measured at the end the waveguide or optical path, which prevents simultaneously sensing multiple analytes on a single waveguide. This paper describes recent work on a novel planar dielectric-waveguide-based local evanescent array-coupled (LEAC) sensor. The immunoassay mechanism of the LEAC sensor relies on specific binding of analytes or targets to one of several localized regions of immobilized biological molecular probes, such as antibodies or ssDNA, to modify the waveguide cross section, and thus, local evanescent fields both above and below the waveguide, as illustrated in Fig. 1 and discussed in Section II-A. Compared to SPR biosensors or ring/disk resonator biosensors, the LEAC biosensor is a nonresonant device with minimal temperature dependence. Furthermore, it does not require a laser source but can be operated with LEDs that offer both noise and system simplification advantages. Narrow-beam-divergence superluminescent LEDs may be particularly attractive for this application [12]. An entire multianalyte LEAC system including optical source, detector array, integrated signal processing, and telemetry electronics with a simple capillary-force-driven microfluidics system should occupy a volume $<1 \text{ cm}^3$.

This paper is organized into sections on the principles of operation, experimental methods, data analysis and discussion, and conclusions. In Section II, the principles of the local evanescent field shift mechanism will be reviewed and beam propagation method (BPM) simulation results will be used to discuss

the relationship between the light intensity modulation ratio and adlayer thickness for different detector positions below the waveguide core. Section III presents experimental techniques, including fabrication and preparation of integrated sensor chips, sensor readout methods (near-field scanning optical microscopy (NSOM) and buried detector arrays), and thin-film patterning on the waveguide. Results and analysis of the experiments confirming the LEAC sensor concept, validating the operation of the buried detector architecture, demonstrating sensitivity to single nanometer thick biological adlayers, and substantiating low interference from operating temperature changes are discussed in Section IV. It includes a summary of recent studies on variable analyte concentration immunoassay complex layers using NSOM [13] as well as details on the electronic response of CMOS chips with integrated photodetectors to thinned photoresist and patterned bovine serum albumin (BSA) layers [14].

II. LEAC BIOSENSOR CONCEPT

A. Local Field Shift Principle

Increased local refractive index at the waveguide's upper surface due to the formation of a biological adlayer shifts the evanescent field distribution up, and hence, changes the evanescent optical intensity both above and below the waveguide structure in the LEAC biosensor. The principle is illustrated in Fig. 1 on a proof-of-concept structure consisting of a shallow ridge waveguide made from a SiN_x core over a lower cladding of SiO_2 . Nanoscale organic layers, such as those formed by the binding of target antigens or antibodies, increase the effective refractive index just above the silicon nitride waveguide core, and hence, shift the evanescent field profile up. The evanescent field shift can be detected by an NSOM above the waveguide or buried detector arrays positioned below the waveguide. To increase the light intensity modulation caused by a thin film on the waveguide surface, an asymmetric ridge waveguide structure is employed where the lower cladding has a higher index than the upper cladding and the core thickness is small enough to place the waveguide close to cutoff. As molecules bind to the upper surface of the thin core, the effective refractive index of the upper cladding increases, thus causing both an upward shift in the guided mode as well as tighter optical confinement, which increases the evanescent field decay constant in the lower cladding. The light intensity modulation ratio is

$$\frac{\Delta I}{I_0} \approx \frac{\exp(-2\gamma_{\text{ad}}s) - \exp(-2\gamma_0s)}{\exp(-2\gamma_0s)} = \exp(-2(\gamma_{\text{ad}} - \gamma_0)s) - 1 \quad (1)$$

at a distance s below the waveguide core in response to the adsorption of an adlayer that shifts the evanescent field decay constant from γ_0 to γ_{ad} . The normalized photocurrent modulation of a thin linear detector will be approximately the same as the intensity modulation ratio. For very thin adlayers, $\Delta I/I_0 \approx -2(\gamma_{\text{ad}} - \gamma_0)s$, which makes the normalized response proportional to the detector distance from the core. Positioning a detector further from the waveguide core increases the modulation ratio and can lead to large percentage changes in photocurrent for nanoscale changes in layer thickness, thus

providing high sensitivity. The evanescent decay constant specifying field penetration into the cladding varies along the waveguide according to the adlayer thickness in that region, so that a photodetector array can sense varying adlayer thicknesses like those resulting from different levels of specific binding along the waveguide.

While the modulation ratio increases with s , detectors farther from the core intercept less power leading to a tradeoff in maximizing the signal to noise ratio (SNR) in the case of fixed power in the waveguide. Considering the shot noise, $i_{\text{shot}}^2 = 2qRP_0 \Delta f$, for a measurement bandwidth Δf using a buried detector with responsivity R that intercepts a power P_0 in the absence of an adlayer, the SNR of the system for small changes in adlayer thickness causing a photocurrent RP_{ad} is

$$\text{SNR} = \frac{R^2(P_{\text{ad}} - P_0)^2}{i_{\text{shot}}^2} = \frac{2[(\gamma_{\text{ad}} - \gamma_0)s]^2}{q\Delta f} RP_{\text{WG}} e^{-2\gamma_0s} \quad (2)$$

where q is the elementary charge, $P_0 = P_{\text{WG}} \exp(-2\gamma_0s)$ and P_{WG} is the equivalent power intercepted by a buried detector photocurrent for $s = 0$, which is proportional to the optical power in the waveguide. The shot-noise-limited SNR reaches its maximum value of $\text{SNR}_{\text{max}} = (2/e^2)(\gamma_{\text{ad}}/\gamma_0 - 1)^2 RP_{\text{WG}}/q \Delta f$, when $s = 1/\gamma_0$. Fixed levels of amplifier noise would make the optimum separation $s = 1/2\gamma_0$, one-half of the value for the shot-noise-limited case since the noise is no longer proportional to P_0 . The initial value of γ_0 can be made arbitrarily small by operating as close to cutoff of the asymmetric waveguide as allowed by manufacturing tolerances. Typical calculated values are $\gamma_0 \approx 1.7 \mu\text{m}^{-1}$ for the conservative waveguide design with a silicon nitride core thickness of 100 nm in the experiments discussed in Section IV. However, for these experiments, detector separations of $s > 1/\gamma_0$ were used. A silicon nitride core thickness of 80 nm, pushing the waveguide closer to cutoff, lowers the calculated decay constant to $\gamma_0 \approx 0.2 \mu\text{m}^{-1}$. It is emphasized that SNR can be arbitrarily increased by launching more optical power into the waveguide and thus increasing P_{WG} in the shot or fixed-amplifier noise cases. While increasing guided power does not help in the case that source noise dominates, SNR increases monotonically with increasing s in that situation. A further benefit of large detector separations and the resulting large modulation ratios is a decreased requirement of the dynamic range of readout electronics. For example, the impact of quantization noise for a fixed bit count in appropriately scaled analog-to-digital converters will be reduced with larger values of s . Scattered light from the waveguide will also affect the detector array photocurrents and may be significant for large detector separation. However, knowledge of the waveguide scattering loss from reference regions allows calculation of the expected contribution from scattering that can be subtracted from the measured photocurrent signals.

B. Simulation Results

The nonlinear response of the waveguide-based sensor structure has been modeled by computing intensity modulation ratio using the BPM. The equilibrium intensity on the adlayer surface

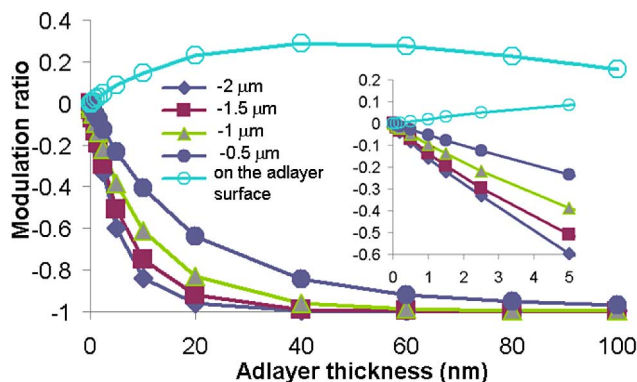


Fig. 2. Modulation ratio from BPM simulations as a function of adlayer thicknesses at the top surface of the adlayer (open circles) and for different vertical positions below the waveguide (closed symbols). The inset shows a magnified view for thin adlayers on similar axes as those in the main plot.

and at different depths below the waveguide core was simulated for varying thicknesses of adlayers with a refractive index of 1.55, as expected for proteins. The modulation ratios due to the change in intensity from the case with no adlayer are plotted in Fig. 2. For an adlayer thickness of 1 nm, the light–intensity modulation on the waveguide and adlayer surface, approximating the case of NSOM measurements, is expected to be 2%, while the modulation ratio 1.5 μm under the waveguide, corresponding to a buried photodetector, is predicted to be 16%. Thus, numerical simulations predict that much larger modulation ratios can be obtained using buried detector arrays and this trend is confirmed by the following experimental results. While the sensor’s nonlinear response to organic adlayer thickness slightly complicates calibration, which can be easily implemented with future on-chip electronics, the approximately inverse exponential behavior simultaneously offers a lower limit of detection and larger dynamic range. Increasing s improves the limit of detection at the expense of decreased dynamic range, as can be seen in Fig. 2. The biosensor response to adlayer thicknesses is determined by the photodetector position and the waveguide parameters, and could be calibrated by one or two measurements with known concentration to determine the dependence of γ_{ad} on adlayer thickness.

III. EXPERIMENTAL TECHNIQUE

A. Biosensor Fabrication and Preparation

Two kinds of waveguide biosensor samples were fabricated for different readout methods. For the NSOM measurement, a SiN_x – SiO_2 waveguide structure without buried detectors as shown in Fig. 1 was fabricated using traditional sputtering, optical lithography, and etching methods. A 100-nm-thick SiN_x film was deposited on a SiO_2 –Si wafer using NH_3 –argon sputtering, where the thickness of SiO_2 cladding was about 2 μm . The upper cladding is air, which allows the NSOM to reach the evanescent field there. A 2- μm -wide ridge waveguide core was defined by partially dry-etching the surrounding SiN_x layer in a CF_4 – O_2 plasma.

Samples with buried detectors were fabricated using a conventional 0.35 μm CMOS process flow [15] in a commercial

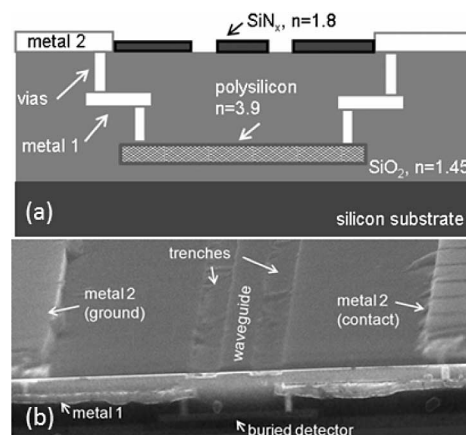


Fig. 3. Cross section and SEM picture of the LEAC biosensor structure incorporating buried detectors.

facility. As shown in Fig. 3(a), a 250-nm-thick polysilicon layer was deposited on a 200-nm-thick field oxide layer on a silicon substrate and used to form the buried photodetector array. Multiple layers of phosphosilicate glass (PSG) and tetraethyl orthosilicate (TEOS) silicon dioxide dual film totaling 1.5 μm in thickness were deposited for intermetal dielectric layers as well as the waveguide’s lower cladding. PSG and TEOS are silicon dioxide with different formations and have the same refractive index of 1.45. A 100-nm-thick SiN_x layer ($n = 1.8$) was used to passivate the integrated circuit chip but also served as the waveguide core. Two 1- μm -wide trench structures were etched in the SiN_x layer to laterally define the 2.3- μm -wide waveguide core structure. The buried detector array was connected to probe pads in metal-2 on the wafer surface by the metal-1 layer and two levels of vias. The lower vias served as contacts to the undoped polysilicon metal–semiconductor–metal photodetectors. The photodetector array elements are 95 μm long and separated from neighboring detectors by 5 μm .

Fig. 3(b) contains SEM images that show both an oblique top view and cross section of the biosensor. The two trenches that were used to laterally define the waveguide were very rough. Strong waveguide sidewall scattering was expected from this SEM examination and was confirmed from experimental data, including very large waveguide loss values.

The integrated sensor chips were fiber-coupled and tested with different sensing region materials to establish their response. First, the waveguide end-facets at the edges of individual die were polished for end-fire coupling of a 654 nm laser diode via visible single-mode fiber (4/125 μm core/cladding diameter). A pair of probe needles applied voltage bias between one of the individual detector pads and the common ground pad, creating an electric field oriented perpendicular to the direction of light propagation. The photocurrent for that detector was measured using either an HP4145 semiconductor parametric analyzer or a K2400 source meter before moving the probe needle to the next detector pad and repeating the photocurrent measurements sequential for each detector. Due to mode mismatch between the output of the 4- μm -core-diameter fiber

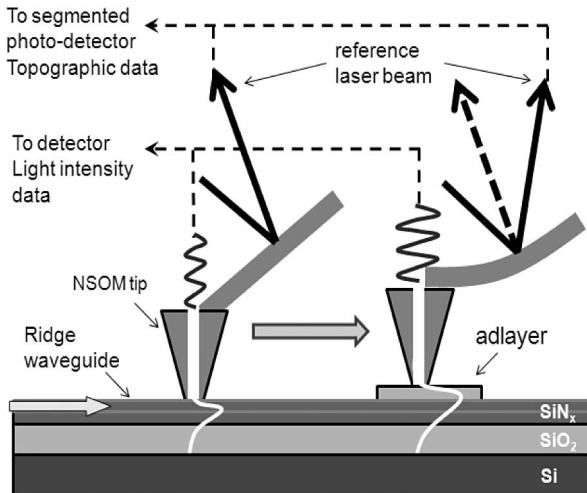


Fig. 4. Structure of the NSOM used for optical and topographic imaging of waveguide samples.

and the $1\ \mu\text{m}$ mode field diameter of the waveguide, coupling efficiency was low and approximately $10\ \mu\text{W}$ was coupled into the waveguide.

B. Biosensor Readout

In order to analyze the local evanescent field shift mechanism in a proof-of-concept configuration without the underlying detector array, NSOM was used to directly measure the evanescent field on the upper surface of the waveguide. The NSOM technique has been frequently used for optical waveguide characterization of light propagation properties, spatial mode profiles, and guided mode interference [16]. An Alpha-NSOM system from WiTec was employed that has simultaneous optical and topological profiling capability. The experimental setup is shown in Fig. 4. The NSOM tip is a hollow aluminum pyramid integrated on a Si cantilever that converts the evanescent field to a propagating wave, which will be detected by a photomultiplier tube. A reference laser beam reflecting off the cantilever is directed to a quadrant detector by a dichroic beam splitter and is used to sense tip deflection. To measure the field at the top surface of the waveguide, the NSOM was operated in contact mode.

Similar to an NSOM, a buried detector array directly measures the evanescent field strength and thus the optical intensity, but below the waveguide. While NSOM serves as a powerful investigative tool for understanding the local field shift mechanism on simplified samples, sensing with an integrated photodetector array results in a much larger light intensity modulation ratio. Of course, the use of an integrated photodetector array also eliminates the need for large instrumentation such as that involved with NSOM and allows for an integrated optoelectronic system-on-a-chip. The greater sensitivity and system miniaturization provided by buried detectors are critical for application of the LEAC sensor in ambulatory, field-deployable, or point-of-care devices.

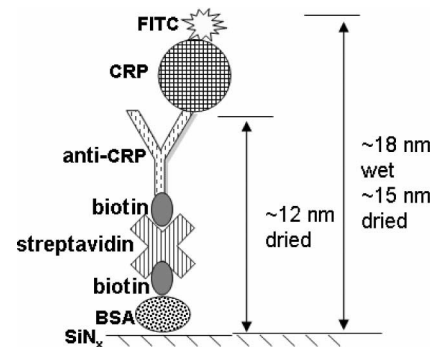


Fig. 5. Fluorescently labeled CRP/anti-CRP immunoassay complex. The biotinylated anti-CRP is functionalized to the surface of the silicon nitride waveguide using biotinylated BSA and streptavidin.

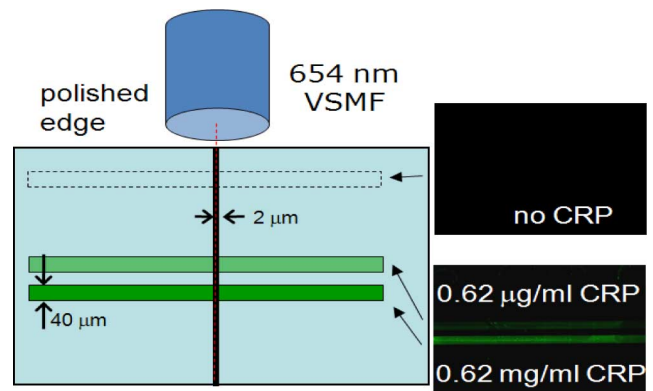


Fig. 6. Three adlayer regions formed with different CRP concentrations across the waveguide. Fluorescent intensity was used to verify CRP binding but was not required for the LEAC sensor.

C. Biosensor Patterning

In an experiment performed with NSOM, adlayers composed of a multiple component immunoassay complex were patterned on the waveguide surface. The adlayer consisted of biotinylated BSA, streptavidin, anti-C-reactive protein (CRP) and CRP layers, as illustrated in Fig. 5. Each component of the immunoassay complex was attached to the surface by sequentially flowing an associated solution through microchannels in a polydimethylsiloxane (PDMS) mask temporarily attached to the sample surface [17], [18]. Three separate $40\text{-}\mu\text{m}$ -wide channels were used to form 11.6-, 12.4-, and 14.8-nm-thick adlayers across a common waveguide, as illustrated in Fig. 6, by using different concentrations of CRP in solution ($0\ \mu\text{g}/\text{mL}$, $0.6\ \mu\text{g}/\text{mL}$, and $0.6\ \text{mg}/\text{mL}$) in the three channels. After adlayer formation, the PDMS pieces were removed and the biofilms were dried in air prior to NSOM measurements. The PDMS blocked the formation of adlayers outside the channels. To help visualize the pattern, the CRP was labeled with fluorescein isothiocyanate (FITC), although this is unnecessary for the LEAC sensor detection.

Experiments were also performed on buried detector chips with patterned organic layers consisting of either thinned photoresist or adsorbed BSA. In order to pattern a thin layer of photoresist on a chip, AZ5214-E photoresist diluted in

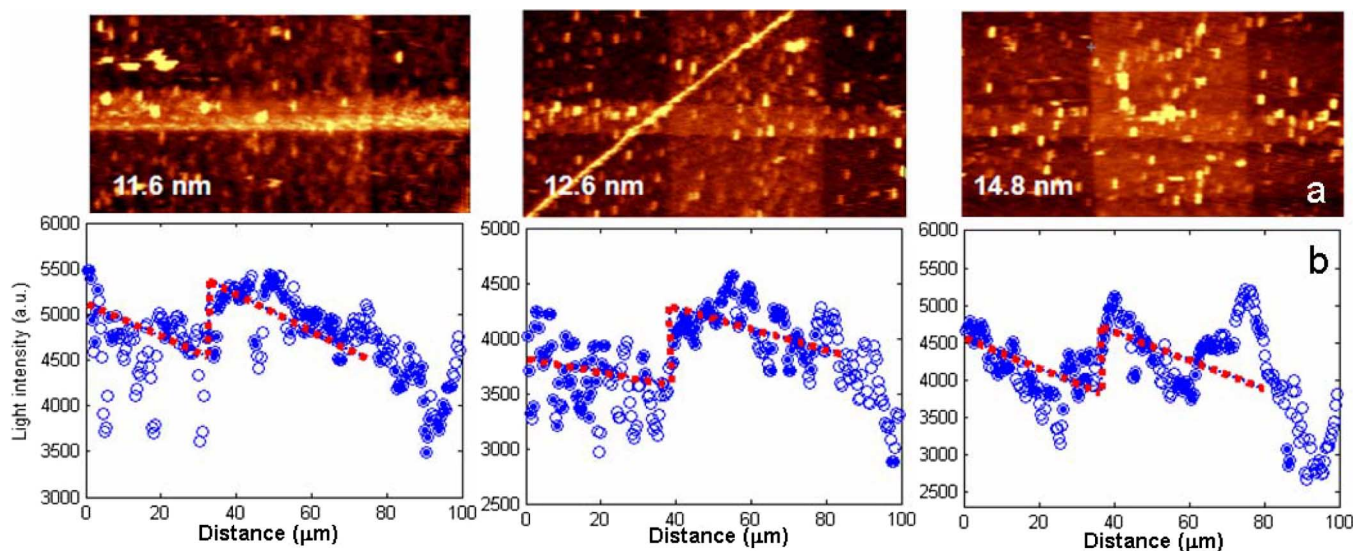


Fig. 7. (a) Topography scans ($15\ \mu\text{m}$ tall $\times 100\ \mu\text{m}$ wide) of three different thicknesses of CRP immunocomplex adlayers obtained using different concentrations of CRP. (b) Light intensities along the waveguide for clean areas (filled circles) and topographic high points that are not included in the fit (open circles).

propylene glycol methyl ether acetate (PGMEA) was employed. The AZ5214-E:PGMEA (1:4) solution was spun on the sample at 6000 r/min for 30 s. The sample was then soft-baked at $95\ ^\circ\text{C}$ for 1 min to drive off the remaining solvent. Next, the photoresist layer was exposed with $10\ \text{mW}/\text{cm}^2$ 405 nm UV light for 45 s after aligning a photomask with 200- or $600\text{-}\mu\text{m}$ -wide features on the desired photodetectors. The sample was developed via immersion in AZ400K:H₂O (1:4) solution for 5–10 s. Postbaking the sample at $100\ ^\circ\text{C}$ for 1 min hardens the photoresist after developing. Topographic analysis showed that the photoresist was 120 nm thick. This patterning was used to test the response of the LEAC sensor to uniform thin adlayer, and 120 nm photoresist film is the thinnest film we could get in our clean room.

In the last experiment, a BSA layer was directly adsorbed onto the surface of a waveguide sensor with buried detectors. To aid visualization of the pattern, BSA was fluorescently labeled with FITC, obtained from Sigma, according to manufacturer's protocol. FITC-BSA patterning was achieved by using a PDMS mask with a circular reservoir structure. A solution of 1 mg/mL FITC-BSA in phosphate-buffered saline (PBS) was delivered into the reservoir after the PDMS mask was applied to the sample surface. The PBS solution comprised 50 mM sodium phosphate, 150 mM sodium chloride, 0.05% Tween 20, in deionized water, and adjusted to pH 7.4. Once delivered to the die surface, FITC-BSA solution was incubated for 20 min at room temperature in a humidity-controlled chamber. Following incubation, the mask was removed and die was rinsed with PBS, then deionized water, and dried under nitrogen gas.

IV. RESULTS AND ANALYSIS

A. NSOM Measurement Results

In order to investigate the effect of an adlayer increasing the refractive index above waveguide on the evanescent field distribution, samples without buried detector arrays were tested

with the immunocomplexes shown in Fig. 5. NSOM was used to directly measure both the topography and optical intensity response of the waveguide to the three different adlayer thicknesses. A large number of processing defects, residue spots, dust particles, or other contaminants were found on the sample surface, which appear as bright spots in the false intensity topographic images shown in Fig. 7(a). During the NSOM scanning, these high points lift the NSOM tip away from the main surface, but are too small to significantly affect the local evanescent field distribution, and thus decrease the optical intensity at these points. As a result, the optical intensities averaged across the waveguide width as shown in Fig. 7(b) have sharp dips correlated with the bright spots that occur on the waveguides. To improve data analysis of the intensity profiles, intensity data were excluded at positions corresponding to topological points more than 4 nm above the waveguide ridge and adlayer, which are shown with open circles in Fig. 7(b). The remaining filtered data are shown with the solid circles. Least-squared linear fits, shown with the dotted lines, are made to the filtered data in the region before and within each adlayer region to determine the optical modulation, i.e., increase in measured average intensity associated with each adlayer thickness. The local evanescent field modulation increases with increasing adlayer thickness, as tabulated in Table I. The adlayer thicknesses are obtained from the NSOM topographic measured results. The total adlayer thickness varies by ~ 3 nm, corresponding to the dimensions of CRP, and results in a 5% difference in intensity modulation.

Field responses of the ridge waveguide structure to different adlayer thicknesses were calculated using 2-D BPM simulations. The simulation results show a difference in light intensity modulation ratio of $\sim 5\%$ for the 3 nm adlayer thickness change, which is consistent with the measured results. As in many scanning probe measurements, it is possible that the probe modifies the field, but the excellent agreement between NSOM data and BPM simulation results on similar samples, including mode beating [13], offers confidence that the NSOM measurement

TABLE I
ADLAYER THICKNESS AND INTENSITY MODULATION

| CRP Concentration | Adlayer Thickness | Measured Intensity Modulation | Simulated Intensity Modulation |
|----------------------|-------------------|-------------------------------|--------------------------------|
| 0 $\mu\text{g/ml}$ | 11.6 nm | 18.2% | 21.0% |
| 0.6 $\mu\text{g/ml}$ | 12.4 nm | 19.9% | 22.2% |
| 0.6 mg/ml | 14.8 nm | 23.3% | 25.8% |

does not significantly perturb the evanescent field distribution. However, the absolute value of the measured light intensity modulation ratio is $\sim 2\%$ lower than the simulated results. This slight difference may be caused by the rough topology increasing the effective distance of the NSOM tip to the waveguide surface.

B. Buried Detector Array Measurement Results

To interrogate the effects of an increase in refractive index due to the addition of an adlayer at the surface of waveguides on the evanescent field shift below the waveguide, CMOS chips with buried detector arrays were tested using patterned regions of thinned photoresist as well as adsorbed layers of BSA. Photocurrents were initially measured on bare chips before the organic layers were deposited and patterned to record a baseline and measured again afterward to determine the photocurrent modulation ratio caused by the adlayer. Light was incident from the side of the chip near detector #1 and propagated past higher numbered detectors. The detector elements before the patterned region are expected to have similar photocurrents before and after patterning, corresponding to a near zero modulation ratio, while the drop in photocurrents under the patterned region amounts to a negative modulation ratio, as defined in (1).

The first experiment on an integrated sensor chip had a 200- μm -long, 120-nm-thick photoresist layer patterned across the waveguide above the ninth and tenth buried detectors, as shown in Fig. 8(a). Measured photocurrents from detector array elements before photoresist coating, plotted with open squares in Fig. 8(b), are proportional to the light in the guided mode and exponentially decrease along the waveguide as the power in the waveguide is attenuated.

The modulation ratio for each detector observed after photoresist patterning is shown with circles in Fig. 8(b). The ratio decreases from approximately 0 to -0.55 , i.e., the photocurrent decreases by 55%, due to the patterned photoresist film at the 10th photodetector, before rising back to $+0.27$ at the 11th detector. These results imply that the light field is shifted up at the waveguide location where there is photoresist ($n = 1.55$), and hence, the photocurrent in the buried detector under the waveguide decreases at that location. The modulation ratio beyond the photoresist is higher than the ratio before the photoresist due to reduced absorption by the photodetectors under the photoresist, leaving more light in the waveguide after the photoresist region.

The minimal decrease in photocurrent of the ninth photodetector may be due to light scattering by the edge of the relatively

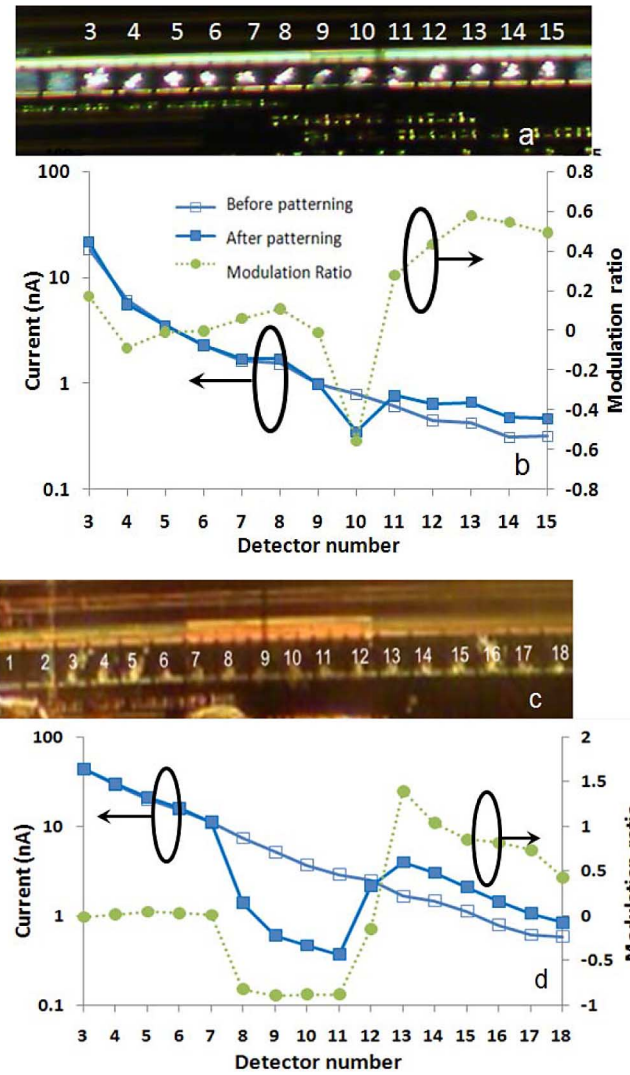


Fig. 8. (a) Photograph of a LEAC sensor waveguide with 200- μm -long photoresist patterned above the ninth and tenth detectors. (b) Photocurrents measured before (open squares) and after (squares) the photoresist is patterned as well as the modulation ratio (dotted line). (c) Photograph of a LEAC sensor waveguide with 600- μm -long photoresist patterned above the 7th and 12th detectors. (d) Photocurrents measured before (open squares) and after (squares) the photoresist is patterned as well as the modulation ratio (dotted line).

thick 120 nm photoresist film, but the return of the photocurrent to higher levels beyond the photoresist indicates that the large current decrease for the tenth detector is not caused by greatly reduced power in the waveguide. Although the simulation shows that the modulation should be larger than 90%, the measured modulation ratio is approximately 55% at the tenth detector. Several factors may cause this difference. First, as described before, the field distribution will shift upward when an adlayer forms on the waveguide, increasing the fraction of optical power in the core (i.e., increasing the confinement factor), and hence increasing scattering due to sidewall roughness of the core. Second, the abrupt transition out of the thick adlayer will also cause strong backscattering near detector #10 when light exits the adlayer region. Third, the lower index contrast between the cladding and core also reduces scattering due to sidewall

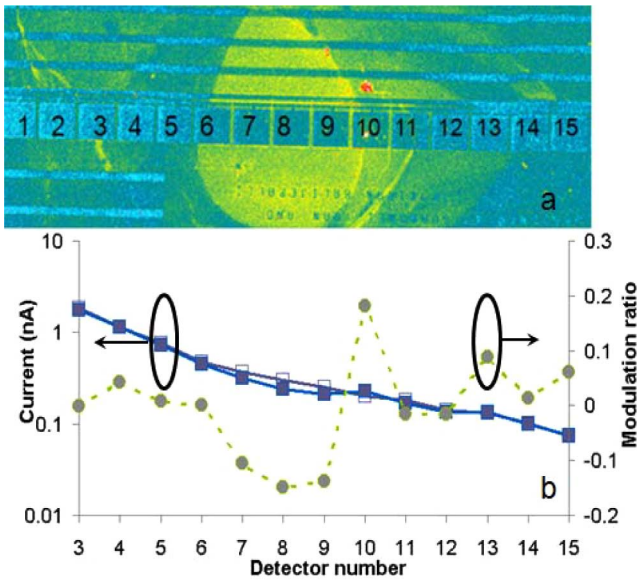


Fig. 9. (a) Photograph of a LEAC sensor waveguide with BSA patterned above the 6th and 14th detectors. (b) Photocurrents measured before (open squares) and after (squares) the BSA is patterned as well as the current ratios (dotted line).

roughness. Scattered light from the first two mechanisms will increase the photocurrents across the detector, and hence, decrease the modulation ratio, while the third mechanism will help to increase the modulation ratio. In this case, considering the thick adlayer (120 nm), the first two mechanisms overcame the last mechanism.

To further investigate the impact of the second mechanism, scattering at the beginning and end of the adlayer, a 600- μm -long photoresist adlayer was patterned across the waveguide above buried detectors #7–#12 of a second chip, as shown in Fig. 8(c). Similarly to the experiment with the shorter photoresist region, decreased photocurrents are measured at the positions where the waveguide is covered by the photoresist adlayer except on the first detector. However, the largest modulation ratio in this case is around 87%, which agrees better with the 99% predicted by the simulation results.

The thinned photoresist adlayer is about 120 nm thick, which is much thicker than expected for immunoassay layers and photocurrent response was near saturation in this case. Thus, the response of the LEAC sensor to a much thinner adlayer was studied in the final experiment.

A BSA film, whose thickness was two orders of magnitude smaller, was patterned on the waveguide of another chip above four photodetectors (#6 through #9). BSA was labeled with FITC to aid visualization of the pattern, as shown in Fig. 9(a), and correlate the relative amount of adsorbed BSA. Based on calibration of fluorescence intensity proportional to layer thickness and an atomic force microscope (AFM) thickness resolution of approximately 1 nm, the effective thickness of the BSA film was determined to be 1 nm or less. Since adsorbed BSA molecules typically have thicknesses of 2–3 nm [19], the effective thickness corresponds to a surface coverage of less than 50%. The low concentration of FITC-labeled BSA in con-

junction with the moderate evanescent field strength on the top surface is not expected to cause significant changes in the absorption of the guided light. This was confirmed by the observation of similar waveguide decay constants with and without FITC labeling of the BSA.

As was observed in the experiments on photoresist, the modulation ratios at the first and last detectors were still affected by light scattering. However, the maximum modulation ratio of approximately -15% at the eighth detector was in better agreement with the BPM-simulated modulation ratio of -16% for a 1-nm-thick layer. Smoother sidewalls in an improved waveguide structure will decrease sidewall scattering and should help to further decrease the difference between simulated and measured results.

In the experiment, the relative photocurrent noise level, which is primarily attributed to source and coupling amplitude noise, was approximately 10% using a 5-Hz measurement cycle. For thin adlayers (<5 nm), the sensitivity of the LEAC sensor is about 15%/nm, which suggests that the limit of detection is approximately 0.4 nm/Hz. Based on topology data for CRP shown in Table I, 0.6 $\mu\text{g}/\text{mL}$ corresponds to a layer thickness of 0.8 nm, which is taken to be in the linear region of the CRP:anti-CRP association curve. This translates to an estimated limit of detection of approximately 3 $\mu\text{g}/\text{mL}$ for a 100-s integration time. The noise could be greatly reduced in ac-modulated detection to avoid 1/f noise and could be further decreased by using reference waveguide regions with no binding to compensate for the source amplitude fluctuation and thermal drift.

C. Temperature Dependence

As temperature dependence is of primary concern in the calibration and application of biosensors, particularly under point-of-care conditions, the temperature dependence of the LEAC sensor was analyzed. Since the LEAC sensor does not rely on a resonance, it is much less sensitive to temperature changes than other types of evanescent waveguide sensors incorporating resonators. The maximum rate of change in transmission, Tr , at a fixed wavelength in a Lorentzian resonance, as the resonant wavelength, λ_{res} , tunes, has a magnitude of $|d\text{Tr}/d\lambda_{\text{res}}| = (\sqrt{27})/(4\Delta\lambda_{\text{FWHM}})$ and occurs at the steepest points on each side of a unit magnitude peak. The full-width at half-maximum of the peak is $\Delta\lambda_{\text{FWHM}}$. Since the resonance wavelength shifts with temperature T according to $d\lambda_{\text{res}}/dT = \lambda_{\text{res}}dn/dT$, where n is the refractive index, the chain rule provides that the maximum rate of change in transmission with temperature is

$$\frac{d\text{Tr}}{dT} = \frac{d\text{Tr}}{d\lambda_{\text{res}}} \frac{d\lambda_{\text{res}}}{dT} = \frac{\sqrt{27}}{4} Q \frac{dn}{dT} \quad (3)$$

where Q is the Q -factor. Although the transmission at other points on the lineshape shift more slowly, they also have less impact on curve fits that determine the position of the transmission peak. Ring and disk resonator structures purposely employ very large Q -factors to obtain high sensitivities, but this results in extreme temperature dependence requiring very well matched reference resonators. For example, Suter *et al.* described a ring

resonator biosensor with $Q = 10^6$ and a measured temperature-dependent wavelength shift of 10 or 20 pm/C for aluminosilicate or fused silica waveguides, respectively [20], which is consistent with published values of $dn/dT \sim 10^{-5}$ [21]. The resulting change in transmission with temperature for such a high- Q resonator would be as high as 1300%/°C. For a typical nonresonant biosensor such as the Mach-Zehnder interferometer described in [22], the temperature needs to be stabilized within 0.03 °C to achieve a 0.1 nm resolution in adlayer thickness.

To investigate the temperature effects on the LEAC sensor, a photoresist-patterned sample was mounted on a thermal electric cooler whose temperature was monitored by an IC temperature transducer (AD590) placed on the sensor chip. The measured modulation ratio magnitude change was $-0.3\% \pm 0.15\%/^{\circ}\text{C}$ across the temperature range of 20 °C–30 °C. This change could be attributed to the index change of the photoresist ($dn/dT = -1.1 \times 10^{-4}$) [22], but in any case is more than three orders of magnitude smaller than for a ring resonator with $Q = 10^6$.

V. CONCLUSION

In this paper, a novel LEAC biosensor has been demonstrated. BPM simulations confirmed the proposed operating mechanism and the increased sensitivity of buried detectors with large separations from the core. NSOM was used to directly study the light field response of the LEAC biosensor to CRP immunocomplexes with different concentrations and 5% modulation ratio was measured for a 3 nm adlayer thickness change, which agreed well with the simulation result. Samples with integrated buried detector arrays were characterized with both the thinned photoresist and a ~ 1 -nm-thick BSA nanofilm. For the BSA film, a very high sensitivity of 15%/nm was demonstrated. Lastly, experimental measurements established the low temperature dependence of the LEAC sensor. These characterizations show that the LEAC biosensor has good potential to be a practical label-free chip-scale system for inexpensive but sensitive detection of immunoreactions.

ACKNOWLEDGMENT

The authors would like to thank R. Pownall, C. Thangaraj, T. Chen, and P. Nikkel for design and fabrication of sensor chips with buried detectors; M. D. Stephens and D. S. Dandy for fabrication of NSOM samples and NSOM measurements; X. He, B. Murphy, and C. Henry for patterning CRP/anti-CRP complexes and provision of reagents; A. Van Orden for access to NSOM instrumentation; and J. Sambur and B. Parkinson for AFM measurements.

REFERENCES

- [1] M. Weisser, G. Tovar, S. Mittler-Neher, W. Knoll, F. Brosinger, H. Freimuth, M. Lacher, and W. Ehrfeld, "Specific bio-recognition reactions observed with an integrated Mach-Zehnder interferometer," *Biosens. Bioelectron.*, vol. 14, pp. 405–411, Apr. 1999.
- [2] R. G. Heideman and P. V. Lambeck, "Remote opto-chemical sensing with extreme sensitivity: Design, fabrication and performance of a pigtailed integrated optical phase-modulated Mach-Zehnder interferometer system," *Sens. Actuators B: Chem.*, vol. 61, pp. 100–127, Dec. 1999.

- [3] R. Horváth, H. C. Pedersen, N. Skivesen, D. Selmececi, and N. B. Larsen, "Optical waveguide sensor for on-line monitoring of bacteria," *Opt. Lett.*, vol. 28, pp. 1233–1235, Jul. 2003.
- [4] M. Lee and P. Fauchet, "Two-dimensional silicon photonic crystal based biosensing platform for protein detection," *Opt. Exp.*, vol. 15, pp. 4530–4535, 2007.
- [5] M. Malmqvist, "Biospecific interaction analysis using biosensor technology," *Nature*, vol. 361, pp. 186–187, Jan. 1993.
- [6] R. D. Harris and J. S. Wilkinson, "Waveguide surface plasmon resonance sensors," *Sens. Actuators B: Chem.*, vol. 29, pp. 261–267, Oct. 1995.
- [7] J. Rooney and E. Hall, "Designing a curved surface SPR device," *Sens. Actuators B: Chem.*, vol. 114, pp. 804–811, Apr. 2006.
- [8] R. W. Boyd and J. E. Heebner, "Sensitive disk resonator photonic biosensor," *Appl. Opt.*, vol. 40, pp. 5742–5747, Nov. 2001.
- [9] K. De Vos, I. Bartolozzi, E. Schacht, P. Bienstman, and R. Baets, "Silicon-insulator microring resonator for sensitive and label-free biosensing," *Opt. Exp.*, vol. 15, pp. 7610–7615, 2007.
- [10] M. Sumetsky, R. Windeler, Y. Dulashko, and X. Fan, "Optical liquid ring resonator sensor," *Opt. Exp.*, vol. 15, pp. 14376–14381, Oct. 2007.
- [11] N. M. Hanumegowda, C. J. Stica, B. C. Patel, I. White, and X. Fan, "Refractometric sensors based on microsphere resonators," *Appl. Phys. Lett.*, vol. 87, pp. 201107–201113, Nov. 2005.
- [12] H. Okamoto, M. Wada, Y. Sakai, Y. Kawaguchi, Y. Kondo, Y. Kadota, K. Kishi, and Y. Itaya, "Narrow beam 1.3 μm superluminescent diode with butt-jointed selectively grown spot size converter," *Electron. Lett.*, vol. 33, pp. 811–812, 1997.
- [13] R. J. Yan, G. W. Yuan, M. D. Stephens, X. He, C. S. Henry, D. S. Dandy, and K. L. Lear, "Evanescent field response to immunoassay layer thickness on planar waveguides," *Appl. Phys. Lett.*, vol. 93, pp. 101110–101113, 2008.
- [14] R. J. Yan, G. W. Yuan, S. Mestas, R. Safaisini, and K. L. Lear, "Demonstration of local evanescent array coupled biosensors with organic nanofilms," in *Proc. 21st Annu. Meeting IEEE Lasers Electro-Opt. Soc. (LEOS 2008)*, pp. 240–241.
- [15] R. Pownall, G. Yuan, T. Chen, P. Nikkel, and K. Lear, "Geometry dependence of CMOS-compatible, polysilicon, leaky-mode photodetectors," *IEEE Photon. Technol. Lett.*, vol. 19, no. 7, pp. 513–515, Apr. 2007.
- [16] G. W. Yuan, M. Stephens, D. Dandy, and K. Lear, "Direct imaging of transient interference in a single-mode waveguide using near-field scanning optical microscopy," *IEEE Photon. Technol. Lett.*, vol. 17, no. 11, pp. 2382–2384, Nov. 2005.
- [17] B. Murphy, X. He, D. Dandy, and C. Henry, "Competitive immunoassays for simultaneous detection of metabolites and proteins using micromosaic patterning," *Anal. Chem.*, vol. 80, pp. 444–450, Jan. 2008.
- [18] X. He, D. Dandy, and C. Henry, "Microfluidic protein patterning on silicon nitride using solvent extracted polydimethylsiloxane," *Sens. Actuators B: Chem.*, vol. 129, pp. 811–817, 2008.
- [19] F. Caruso and H. Mohwald, "Protein multilayer formation on colloids through a stepwise self-assembly technique," *J. Amer. Chem. Soc.*, vol. 121, pp. 6039–6046, 1999.
- [20] J. D. Suter, I. M. White, H. Zhu, and X. Fan, "Thermal characterization of liquid core optical ring resonator sensors," *Appl. Opt.*, vol. 46, pp. 389–396, Jan. 2007.
- [21] T. Toyoda and M. Yabe, "The temperature dependence of the refractive indices of fused silica and crystal quartz," *J. Phys. D: Appl. Phys.*, vol. 16, pp. L97–L100, 1983.
- [22] J. Ingenhoff, B. Drapp, and G. Gauglitz, "Biosensors using integrated optical devices," *Fresenius' J. Anal. Chem.*, vol. 346, pp. 580–583, Jun. 1993.
- [23] W.-G. Jung, S.-W. Kim, K.-T. Kim, E.-S. Kim, and S.-W. Kang, "High-sensitivity temperature sensor using a side-polished single-mode fiber covered with the polymer planar waveguide," *IEEE Photon. Technol. Lett.*, vol. 13, no. 11, pp. 1209–1211, Nov. 2001.

Rongjin Yan (S'09) received the B.S. degree in material science from Fudan University, Shanghai, China, in 2003, and the M.S. degree in solid state electronics from Shanghai Jiaotong University, Shanghai, in 2006. He is currently working toward the Ph.D. degree in electrical and computer engineering at Colorado State University, Fort Collins.

His current research interests include the design and fabrication of photonic biosensors and numerical modeling of optical structures.

Santano P. Mestas (S'98) received the B.S. and M.S. degrees in biochemistry in 1999 and 2007, respectively, from Colorado State University, Fort Collins, where he is currently working toward the Ph.D. degree in biomedical engineering.

His current research interests include photonic biosensors and medical device technology.

Guangwei Yuan received the B.S. degree in physics from the University of Science and Technology of China, Hefei, China, and the Ph.D. degree in electrical and computer engineering from Colorado State University, Fort Collins, in 2008.

He is currently with Avago Technologies in Fort Collins.

Rashid Safaisini (S'07) received the B.S. degree in electrical engineering from Shahid Beheshti University, Tehran, Iran, in 2003, and the M.S. degree in electrical engineering from Amirkabir University of Technology (formerly Tehran Polytechnic), Tehran, in 2006. He is currently working toward the Ph.D. degree in electrical engineering at Colorado State University, Fort Collins.

His current research interests include design, fabrication, characterization, and modeling of vertical-cavity surface-emitting lasers (VCSELs).

Kevin L. Lear (S'83–M'88) received the B.S. degree from the University of Colorado, Boulder, in 1984, and the M.S. and Ph.D. degrees from Stanford University, Stanford, CA, in 1985 and 1990, respectively, all in electrical engineering.

From 1990 to 1997, he was a Senior Member of the Technical Staff, Sandia National Laboratories, Albuquerque, NM. In 1997, he became the Chief Scientific Officer at Micro Optical Devices, Inc., Albuquerque, which was subsequently acquired by Emcore Corporation. In 1999, he joined Colorado State University, Fort Collins, as the Rockwell Anderson Associate Professor of Electrical and Computer Engineering. His current research interests include photonic biosensors and components and systems for high-speed optical communication.

Dr. Lear received an IEEE Lasers and Electro-Optics Society Distinguished Lecturer Award in 1996 for his work on vertical-cavity surface-emitting lasers (VCSELs).